

3 Kinematics of HI Envelopes Associated with Molecular Clouds

4 THUMMIM MEKURIA¹ AND NIA IMARA¹

5 ¹*Department of Astronomy and Astrophysics*
6 *University of California, Santa Cruz CA, 95064, USA*

7 ABSTRACT

8 To investigate the evolution of molecular clouds, we study the kinematics of their atomic hydrogen
9 (HI) envelopes. We identify the HI envelopes associated with 22 star forming regions in the Solar
10 Neighborhood, tracing the molecular and atomic gas via ¹²CO and 21-cm emission, respectively. We
11 make velocity field maps and measure large-scale velocity gradients, Ω of both cloud populations,
12 which we then use to calculate their specific angular momenta, $j \propto \Omega R^2$. The molecular clouds have a
13 median velocity gradient of $9.6 \times 10^{-2} \text{ km s}^{-1} \text{ pc}^{-1}$, and a typical specific angular momentum of $2.7 \times$
14 $10^{24} \text{ cm}^2 \text{ s}^{-1}$. The HI envelopes have a median specific angular momentum of $j_{\text{HI}} \approx 1.5 \times 10^{25} \text{ cm}^2 \text{ s}^{-1}$.
15 On average, $j_{\text{HI}}/j_{\text{H}_2} = 8$, indicating that the angular momentum problem persists. Both populations
16 exhibit a size-specific angular momentum relation consistent with the scaling expected of supersonic
17 turbulence: $j_{\text{H}_2} \propto R^{1.67 \pm 0.23}$, and $j_{\text{HI}} \propto R^{1.36 \pm 0.39}$. We demonstrate that a turbulent cascade of
18 $j \propto R^{1.42 \pm 0.03}$ is present across 4 dex in size, $R \in (10^{-2}, 10^2) \text{ pc}$ in the Solar Neighborhood, by
19 compiling our measurements with previous observations. Finally, we derive the angular momenta of
20 the progenitors to the present-day molecular cloud-atomic envelope systems, and estimate their typical
21 angular momentum redistribution timescales to be $\sim 0.9 \text{ Myr}$.

22 1. INTRODUCTION

23 Large-scale linear velocity gradients are routinely ob-
24 served across molecular clouds and cores (e.g., Kutner
25 et al. 1977; Goodman et al. 1993; Rosolowsky et al. 2003;
26 Imara & Blitz 2011; Imara et al. 2011; Tatematsu et al.
27 2016; Chen et al. 2019; Braine et al. 2020). These gra-
28 dients are often attributed to solid-body rotation, and
29 used to infer the specific angular momentum, $j \propto \Omega R^2$,
30 of these structures (e.g., Goodman et al. 1993; Tatem-
31 atsu et al. 2016). The angular momentum of molecular
32 clouds is of interest because it may have a significant
33 impact on the outcomes of star-formation—e.g., the
34 degree of fragmentation (Machida et al. 2008), the IMF
35 (Shen et al. 2025), and proto-planetary disks sizes (Yen
36 & Lee 2024).

37 Observations and theoretical studies agree that molec-
38 ular clouds form when atomic hydrogen (HI) accumu-
39 lates to surface densities exceeding $10 M_{\odot} \text{ pc}^2$, sufficient
40 to shield the H₂ molecule from dissociation by interstel-
41 lar radiation (Krumholz et al. 2009; Imara & Burkhardt
42 2016; Sternberg et al. 2021; Park et al. 2023). Imara &
43 Blitz (2011, hereafter IB) and Imara et al. (2011, here-
44 after IBB) were the first to compare the dynamics of
45 the molecular and atomic phases of hydrogen involved
46 in the formation of molecular clouds. To do so, they
47 devised a method for identifying the HI associated with

48 molecular clouds using spatial and kinematic criteria.
49 IB studied five star forming regions in the Solar Neigh-
50 borhood, finding that the HI envelopes had an average
51 velocity gradient of $0.04 \text{ km s}^{-1} \text{ pc}^{-1}$. The specific an-
52 gular momenta are then $j_{\text{HI}} \approx 1.9 \times 10^{25} \text{ cm}^2 \text{ s}^{-1}$, 2–5
53 times larger than the specific angular momenta of their
54 corresponding molecular clouds.

55 IBB identified the HI envelopes associated with 45
56 molecular clouds in M33 (Rosolowsky et al. 2003),
57 and measured an average velocity gradient of $\Omega_{\text{HI}} \approx$
58 $0.05 \text{ km s}^{-1} \text{ pc}^{-1}$. They found that the HI envelopes
59 had $j_{\text{HI}} \approx 7.8 \times 10^{25} \text{ cm}^2 \text{ s}^{-1}$, which is on average 27
60 times larger than the specific angular momentum of their
61 corresponding molecular clouds. Both IB and IBB also
62 found that the rotation axes of molecular clouds and
63 HI envelope within a given system tend to be randomly
64 oriented with respect to one another.

65 IBB measured the specific angular momentum of iso-
66 lated HI clouds and found that HI clouds surrounding
67 molecular clouds have higher rotational energies than
68 their counterparts unassociated with molecular emis-
69 sion. The increased shear and rotational energy in the
70 HI envelopes harboring molecular clouds suggests that
71 the molecular clouds play a role in increasing the angular
72 momentum of the atomic gas in their vicinity. Mag-
73 netohydrodynamic simulations corroborate this view,
74 demonstrating that molecular clouds dissipate angular

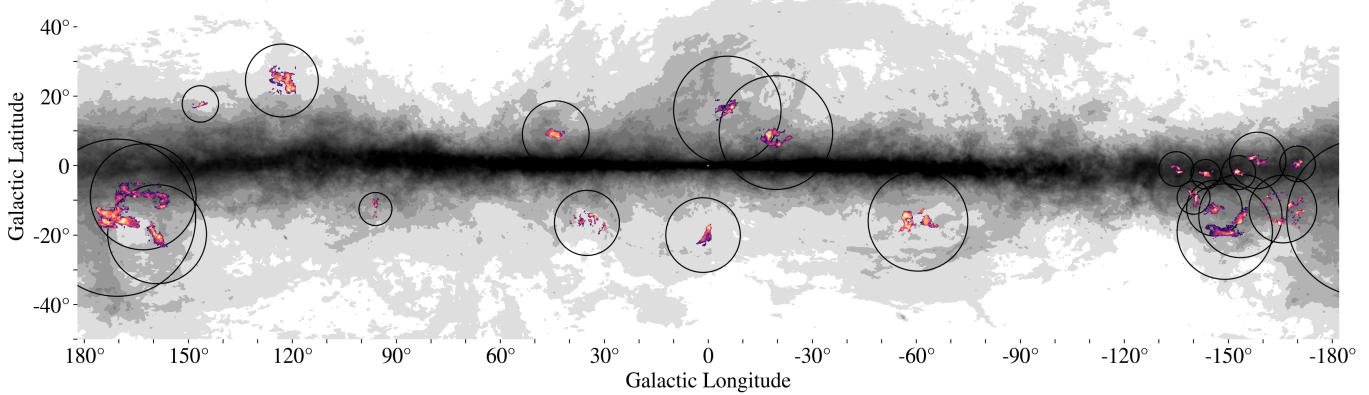


Figure 1. The Solar Neighborhood molecular clouds and their associated HI envelopes studied in this work. The grayscale background map is derived from the zeroth moment of 21-cm emission, and indicates gas with column densities of $N_{\text{HI}} \geq 10^{21} \text{ cm}^{-2}$. The white circles show the radial extent of the HI envelope associated with each molecular cloud (colored contours).

momentum as they evolve (Arroyo-Chávez & Vázquez-Semadeni 2022; Misugi et al. 2024).

Had the molecular clouds formed by simple top-down collapse of atomic gas, the angular momentum of the HI would have been conserved in the molecular clouds. However, IB and IBB demonstrated that neither the magnitudes nor the orientation of the angular momenta of the atomic and molecular gas are aligned. This so-called “angular momentum problem” is a long-standing puzzle (Larson 1981; Rosolowsky et al. 2003; Imara & Blitz 2011; Imara et al. 2011), and has been attributed to gravitational (e.g., Larson 1984), magnetic (e.g., Mouschovias & Paleologou 1979; Misugi et al. 2024), and turbulent (e.g., Vázquez-Semadeni et al. 2024) torques braking molecular clouds during formation.

In this work, we investigate the kinematics of Solar Neighborhood molecular clouds in order to determine whether the findings presented by IB persist with higher resolution and higher sensitivity HI observations—which allow us to capture a larger dynamic range in density—and a sample of clouds that is 4 times larger. We go further than IB, exploring how the specific angular momentum varies in structures ranging 4 orders of magnitude in size, and also estimating the timescale over which angular momentum is redistributed during molecular cloud formation.

The paper is organized as follows: In Section 2, we present the catalog of molecular clouds we study and the observations used to trace molecular and atomic hydrogen. Section 3 describes the spatial and kinematic criteria we use to select the HI envelopes associated with molecular clouds, and we measure the physical properties of each population. Velocity field maps and kinematic properties are presented in Section 4. We quantify population level trends in Section 5. In Section 6, we develop a physical model to follow angular momen-

tum transport in the molecular and atomic phases and contextualize our measurements within the large-scale motion of the Galaxy. We summarize our work in Section 7.

2. DATA

2.1. Molecular cloud sample

We select molecular clouds from the Zucker et al. (2019) catalog of dust-derived distances to Solar Neighborhood molecular clouds. Of the 27 regions targeted in Zucker et al. (2019), we exclude those located at extreme latitudes ($|b| > 30^\circ$) or along lines of sight where the ^{12}CO emission blends with the Galactic plane. The final sample (Table 1, Figure 1) consists of 22 molecular clouds, including the five in Imara & Blitz (2011), as well as other well-studied clouds such as ρ -Ophiuchus, the Polaris Flare, and Corona Australis.

2.2. ^{12}CO observations

The Dame, Hartmann, Thaddeus survey (Dame et al. 2001, hereafter DHT) is the most complete ^{12}CO ($J = 1 \rightarrow 0$) map of the Galaxy, capturing emission at latitudes $\leq 30^\circ$ with an angular resolution of $\theta = 8'.5$. This corresponds to a linear resolution of 0.3 - 4 pc for the cloud distances in our catalog (150 - 200 pc). The velocity resolution of the DHT is $dv = 1.3 \text{ km s}^{-1}$, covering emission within $|v| \leq 300 \text{ km s}^{-1}$ of the 115 GHz line center.¹ Analyses are performed on the moment masked data (Dame 2011).

2.3. 21-cm observations

HI4PI (HI4PI Collaboration et al. 2016) is the highest-sensitivity ($\sigma_{\text{rms}} = 0.43 \text{ mK}$) and highest-resolution

¹ DHT is available as position-position-velocity (ppv) datacubes at <https://lweb.cfa.harvard.edu/rtdc/CO>

($\theta = 16'.2$) 21-cm map of the sky available to date. HI4PI outperforms the LAB survey (Kalberla et al. 2005), which IB use, by a factor of 8 in resolution. We resample the data onto a $0.^{\circ}125$ grid to match DHT.² HI4PI covers emission within $|v| \leq 600 \text{ km s}^{-1}$, at a similar velocity resolution as DHT (1.29 km s^{-1}).³

3. METHODOLOGY

Here we describe the spatial and kinematic criteria used to select the molecular clouds and their associated HI. We then present the physical properties of both molecular clouds and atomic envelopes, and compare with previous findings.

3.1. Identifying the Molecular Clouds

The latitude and longitude ranges that we use to define the boundaries of the molecular clouds (Table 1) are guided by those given in Zucker et al. (2019). Given that we expect ^{12}CO to become optically thick in molecular clouds at a hydrogen column density of about 10^{21} cm^{-2} (Imara & Burkhart 2016), we use this threshold to define the lowest-level contour of the molecular clouds from the ^{12}CO observations. (This is after converting the ^{12}CO brightness temperature into H_2 column density.) For the majority of the clouds in our catalog, we use this column density threshold to mask the data. There are 9 smaller diffuse molecular clouds in our sample with a significant amount of their emission below 10^{21} cm^{-2} ; for these we use a lower cutoff of $\log(N_{\text{H}_2}) = 20.5$.

3.2. Spatial and Kinematic Bounds of HI envelopes

Observations show that molecular clouds in the Milky Way and other Local Group galaxies tend to be spatially and kinematically co-located with thick envelopes of atomic gas having surface densities of $\geq 10 M_{\odot} \text{ pc}^{-2}$ or more (e.g., Imara & Burkhart 2016; Park et al. 2023). For a given molecular cloud, IB and IBB define its HI envelope as the atomic emission located inside a cylindrical volume, “the accumulation region,” surrounding it. The cylinder has a radius R_{HI} , a height of $2R_{\text{HI}}$, and is oriented with its circular faces parallel to the midplane. The accumulation radius, R_{HI} , is set such that the mass of atomic hydrogen, M_{HI} , enclosed within the volume is at minimum equal to the molecular cloud mass, M_{H_2} .

Due to our vantage point in the Galactic Plane, a cylindrical cloud as described above would

² Measurements made using the resampled data are within a few percent of those made using the native resolution data.

³ The data are available as fits and HEALPix cubes at <https://cdsarc.cds.unistra.fr/viz-bin/cat/J/A+A/594/A116#/browse>

cover a solid angle that varies between $4\pi R^2$ and $4\pi\sqrt{2}R^2$, as a function of latitude. This means that HI envelope associated with the highest latitude clouds (in our case, at $b \sim 25^{\circ}$) would cover an area that is $\sim 35\%$ larger than a cloud at the midplane with the same dimensions. This variance in area propagates into calculations of the mass of the HI envelopes and also affects measurements of the velocity gradients. To avoid this, we modify IB’s definition of the accumulation radius by assuming a spherical geometry:

$$R_{\text{HI}} = \left(\frac{3M_{\text{H}_2}}{4\pi n_{\text{HI}} \mu m_p} \right)^{1/3}, \quad (1)$$

where n_{HI} is the number density of atomic hydrogen, μ is the mean molecular weight, m_p is the mass of a hydrogen atom, and M_{H_2} is the molecular cloud mass. We adopt a hydrogen number density of $n_{\text{HI}} = 0.57 \text{ cm}^{-3}$, a typical value for the warm neutral medium (Wolfire et al. 2003). The mean molecular weight is set at Solar metallicity: $\mu = 1.36$.

To identify the atomic gas that is kinematically associated with a given molecular cloud, we start by examining the HI spectrum inside the the accumulation radius R_{HI} . We fit a Gaussian profile to the spectrum to derive the line-center, \bar{v}_{HI} , and linewidth, σ_{HI} . We select 21-cm emission within $\pm 2\sigma_{\text{HI}}$ of \bar{v}_{HI} . In cases where the HI spectrum consists of multiple peaks, the line-center of the corresponding ^{12}CO spectrum is used to select the velocity component associated with the molecular cloud.

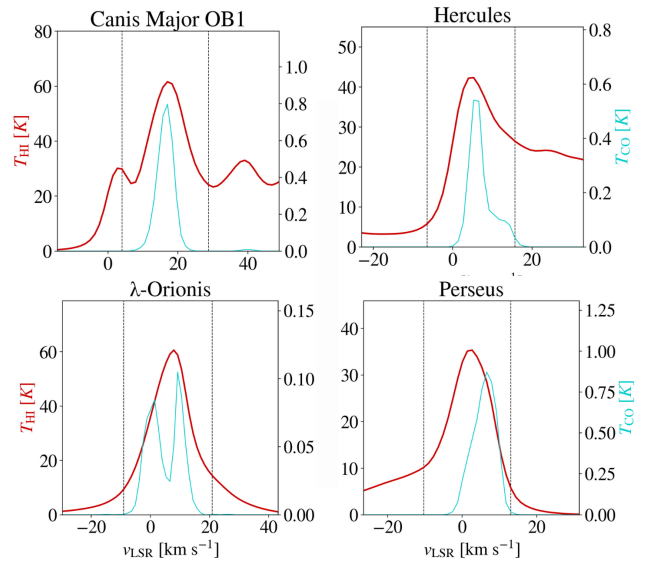


Figure 2. Velocity spectra of molecular clouds (black) and HI envelopes (red). The vertical lines at $\bar{v} \pm 2\sigma_{\text{HI}}$ indicate the range of velocities selected for the HI envelopes.

Table 1. Location and Velocities of Selected Molecular Clouds

Name	l_0	l_1	b_0	b_1	\bar{v}_{HI}	$\sigma_{v,\text{HI}}$	d pc
	deg		deg		km s^{-1}		
Aquila South	41	29	-20	-12	2.4	3.0	133
California	171	155	-13	-2	-0.5	11.6	470
Camelopardalis	150	144	16	19	0.2	3.9	213
Canis Major OB1	-132.5	-138.5	-2.5	1	17.2	6.3	1209
Chamaeleon	-54	-67	-20	-12	1.2	3.9	183
Corona Australis	4	-1	-24	-16	5.9	4.4	151
Crossbones	-138	-142	-12	-6.5	11.8	7.1	886
Gemini OB1	-164	-174	-3	3	6.4	9.9	1786
Hercules	49	41	7	11	5.0	5.6	227
Lacerta	98	94	-18	-8	0.9	5.3	503
Lupus	-14	-27	5	13	2.7	5.6	189
Maddalena	-140.5	-146.5	-5	-0.5	27.6	12.5	2072
Monoceros OB1	-155	-162	-0.5	3.5	8.8	7.3	745
Monoceros R2	-141	-149	-14.5	-10	9.5	6.5	778
Ophiuchus	0	-9	12	19	2.0	4.4	144
Orion A	-141	-155	-21	-16	8.3	6.5	432
Orion B	-149	-158	-17	-10	8.8	6.2	423
λ -Orionis	-159.5	-173	-18	-7	6.7	7.3	402
Perseus	162	155	-26	-16	2.5	5.8	294
Polaris	127	118	20	30	-1.6	9.4	352
Rosette	-151	-155	-3.5	-0.5	11.4	9.6	1304
Taurus	177	164	-20	-11	4.1	8.4	141

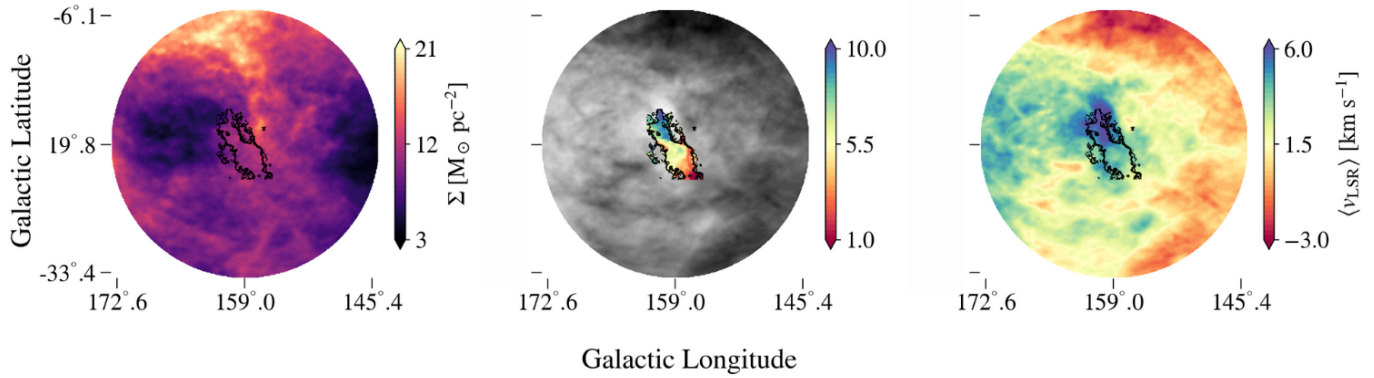


Figure 3. *Left:* Column density map of the HI envelope around the Perseus molecular cloud (black outline). *Middle:* Velocity field maps of the Perseus molecular cloud and (*right*) HI envelope (right), derived from the first moments of ^{12}CO and 21-cm spectral emission. First moment maps of the remaining molecular and HI envelopes are available in the Appendix Maps of the remaining molecular clouds and HI envelopes are available in the Appendix

3.3. Mass and radius

The mass of a molecular or atomic cloud is calculated as

$$M = \mu m_p \sum_{N_{\text{pix}}} N_{\text{H}} dA, \quad (2)$$

where N_{H} is the column density of hydrogen per pixel, and dA is the pixel area. The latter is equal to $(d ds)^2$, where d is the distance and ds is the pixel size. For a molecular cloud, the effective radius is determined from the total ^{12}CO emitting area: $R_{\text{H}_2} = \sqrt{(N_{\text{pix}} dA)/\pi}$.

The molecular clouds column density, N_{H_2} , is derived from the zeroth moment of the ^{12}CO data:

$$N_{\text{H}_2} = X_{\text{CO}} \sum T_{\text{B}}(v) \, dv, \quad (3)$$

where X_{CO} is the metallicity-dependent CO-to-H₂ conversion factor, T_{B} is the brightness temperature, and dv is the velocity resolution. We adopt a value of $X_{\text{CO}} = 1.97 \times 10^{20} \text{ cm}^{-2} (\text{K km s}^{-1})^{-1}$, typical for solar metallicity gas (Lewis et al. 2022). The HI column density is calculated from the 21-cm emission, assuming the optically thin limit (Saha et al. 2018):

$$N_{\text{HI}} = 1.82 \times 10^{18} \sum T_{\text{B}}(v) \, dv \quad (4)$$

The first two columns of Table 2 list the masses and sizes of the molecular clouds and their atomic envelopes. The HI accumulation radii (Equation 1), lie in the range $R_{\text{HI}} \in (19, 150) \text{ pc}$, with a mean of 74 pc. The molecular clouds span $R_{\text{H}_2} \in (4, 43) \text{ pc}$, with an average size of 17 pc.

The molecular clouds cover a large range of masses: $M_{\text{H}_2} \in (580 - 2.7 \times 10^5) M_{\odot}$, with an average of $5.8 \times 10^4 M_{\odot}$ and a median of $2.8 \times 10^4 M_{\odot}$. The HI envelopes have masses in the range $(6.8 \times 10^3 - 3.3 \times 10^6) M_{\odot}$, with a mean of $4.9 \times 10^5 M_{\odot}$ and median of $2.3 \times 10^5 M_{\odot}$.

On average, the HI masses measured from 21-cm emission are 8 times larger than the corresponding molecular cloud mass, which was used to calculate the HI accumulation radius, R_{HI} . A potential reason for this discrepancy could be that i) we underestimated the atomic hydrogen density when calculating R_{HI} , or ii) unrelated HI along the line-of-sight is contributing to the integrated column density N_{HI} . Regarding the former, one could use the denser component of the neutral ISM, with $n_{\text{CNM}} \sim 10^2 n_{\text{WNM}}$, to better trace the HI associated with a molecular cloud. This could be done with maps of HI self-absorption with comparable coverage and resolution to the ¹²CO observations. Line-of-sight distance maps, also of comparable coverage and resolution to the ¹²CO observations, may be to distinguish between the HI envelope and unassociated atomic gas.

4. VELOCITY GRADIENTS

We now derive the velocity fields and large-scale gradients of the molecular clouds and their atomic envelopes.

The velocity gradient Ω is measured from systematic variations in the line of sight velocity field, which maps the intensity-weighted centroid of emission at each pixel.

$$\langle v_{\text{LSR}} \rangle = \frac{\sum v \, T_{\text{B}}(v) \, dv}{\sum T_{\text{B}}(v) \, dv}, \quad (5)$$

Both molecular clouds and their associated HI envelopes are observed to have systematic, near-linear gradients in the velocity fields, often covering the whole extent of the cloud (e.g., Kutner et al. 1977; Goodman et al. 1993; Imara et al. 2011; Braine et al. 2018). We follow Goodman et al. (1993) and calculate Ω by fitting a plane to the first moment maps:

$$v(x, y) = v_0 + \Omega_x(x - x_0) + \Omega_y(y - y_0), \quad (6)$$

where (x_0, y_0) is the center-of-mass of the cloud, v_0 its median velocity, and Ω_x (Ω_y) is the gradient of the first moment map along Galactic longitude (latitude). We determine Ω_x , Ω_y , and v_0 from a least-squares fit; the total magnitude and direction of the velocity gradient are calculated from these parameters as:

$$\Omega = \sqrt{\Omega_x^2 + \Omega_y^2} \quad (7)$$

$$\theta = \tan^{-1}(\Omega_y / \Omega_x). \quad (8)$$

θ is oriented such that the rotation axis of the cloud has a position angle $\phi \equiv (\theta - 90^\circ)$.

The molecular clouds have angular velocities that range in $(0.09 - 0.3) \text{ km s}^{-1} \text{ pc}^{-1}$, with an average of $\Omega_{\text{H}_2} = 0.12 \text{ km s}^{-1} \text{ pc}^{-1}$ and a median of $0.09 \text{ km s}^{-1} \text{ pc}^{-1}$. The HI envelopes have similar velocity gradients as their molecular counterparts, $\Omega_{\text{HI}} \in (0.001 - 0.1) \text{ km s}^{-1} \text{ pc}^{-1}$, with a mean of $0.03 \text{ km s}^{-1} \text{ pc}^{-1}$. Assuming these velocity gradients arise due to solid body rotation, the typical rotational period of the molecular clouds is $2\pi/\Omega \approx 60 \text{ Myr}$, and $\approx 260 \text{ Myr}$ for the HI envelopes. For both populations, this is an order of magnitude larger than the respective mean free-fall time.

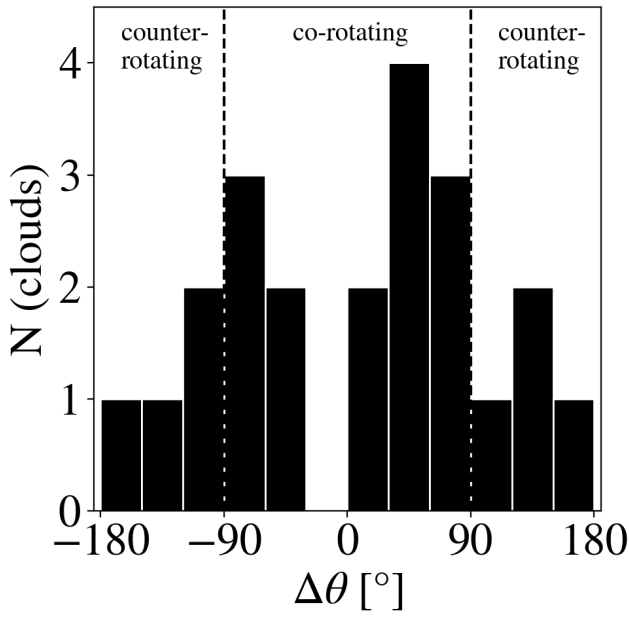
The separation between the rotation axes of a molecular cloud and its corresponding HI envelope is given by $\Delta\theta \equiv |\theta_{\text{H}_2} - \theta_{\text{HI}}|$ (Figure 4). We find that 14 of the molecular clouds are co-rotating ($\Delta\theta < 90^\circ$) with respect to their HI envelope. On the other hand, Imara et al. (2011) find that less than half of the molecular clouds are co-rotating with respect to their HI envelopes. Nevertheless, both agree that there is a relatively uniform distribution of $\Delta\theta$ across all possible values.

4.1. Goodness-of-fit of planar model

In a planar velocity field, the velocity will vary linearly as a function of perpendicular distance from the rotation axis, with a slope equal to Ω . Below, we describe a goodness-of-fit test we performed to determine whether this is a reasonable model for the projected large-scale motion of the gas. We plot the velocity profile for each

Table 2. Physical Properties of Molecular Clouds and HI envelopes in the Solar Neighborhood

Name	M_{H_2}	M_{HI}	R_{H_2}	R_{HI}	Ω_{H_2}	Ω_{HI}	θ_{H_2}	θ_{HI}	j_{H_2}	j_{HI}	p_{H_2}	p_{HI}
	$10^4 M_{\odot}$	$10^5 M_{\odot}$	pc		$10^{-2} \text{ km s}^{-1} \text{ pc}^{-1}$		deg		$10^{24} \text{ cm}^2 \text{ s}^{-1}$			
Aquila South	0.07	0.07	4.4	20.9	7.9	7.6	108.0	116.8	0.19	4.12	0.77	0.94
California	14.37	10.38	32.0	121.4	10.2	8.0	-6.4	-73.6	12.92	146.05	0.99	0.95
Camelopardalis	0.06	0.07	3.6	19.4	10.9	4.4	-103.2	-65.8	0.18	2.04	0.57	0.94
Canis Major OB1	7.97	6.17	23.0	99.8	3.3	1.7	-63.0	82.2	2.19	20.54	0.2	0.86
Chamaeleon	0.82	0.47	9.2	46.8	10.5	0.9	162.7	-166.4	1.08	2.33	0.58	0.2
Corona Australis	0.19	0.15	5.0	28.8	8.8	1.3	135.8	-104.1	0.27	1.33	0.56	0.12
Crossbones	3.11	4.09	22.6	72.9	5.8	4.6	21.0	109.3	3.64	30.48	0.96	0.97
Gemini OB1	27.46	32.86	38.3	150.7	6.0	2.3	-38.3	-19.0	10.79	65.19	0.78	0.98
Hercules	0.46	0.52	7.2	38.5	33.3	4.3	-158.6	-87.4	2.12	7.88	0.65	0.96
Lacerta	0.56	0.53	9.7	41.2	23.0	3.5	26.1	137.9	2.64	7.35	0.94	0.99
Lupus	0.98	1.04	8.7	49.5	16.2	3.4	97.3	72.7	1.53	10.43	0.8	0.62
Maddalena	22.0	11.96	43.0	140	10.7	1.1	75.2	97.1	24.45	26.92	0.93	0.94
Monoceros OB1	8.35	7.18	21.1	101.3	12.1	1.3	92.6	-65.7	6.64	17.04	0.49	0.83
Monoceros R2	9.11	5.94	23.3	104.3	6.4	3.0	-153.5	95.3	4.28	40.17	0.93	0.98
Ophiuchus	0.44	0.51	5.3	38.1	30.5	3.5	-128.1	-57.8	1.06	6.26	0.75	0.81
Orion A	9.01	3.86	20.1	103.9	8.9	1.4	-166.0	104.9	4.44	19.20	0.57	0.3
Orion B	5.42	3.66	13.2	87.8	0.9	1.7	111.6	90.7	0.20	16.50	0.13	0.49
λ -Orionis	2.55	2.9	18.5	68.3	20.6	2.5	83.6	-0.8	8.68	14.64	0.62	0.94
Perseus	3.03	1.51	11.5	72.2	23.9	3.0	24.2	-4.6	3.92	19.57	0.96	0.97
Polaris	2.2	0.82	18.6	64.9	6.7	3.0	-4.2	53.6	2.84	15.52	0.75	0.82
Rosette	8.86	11.13	24.3	103.4	8.7	1.7	-150.5	91.4	6.31	22.42	0.49	0.91
Taurus	1.49	1.64	9.7	57.0	8.4	10.3	-119.2	-54.7	0.97	41.46	0.74	0.98

**Figure 4.** Distribution of angular separations between the rotation axis of molecular clouds and their corresponding HI envelopes.

cloud—both the molecular and atomic gas—as a func-

tion of r_{\perp} (Figure 5). For each profile, we measure the Pearson correlation coefficients, shown in Figure 6 in relation to the velocity gradient position angles.

We find that 77% of the HI envelopes have velocity profiles with correlation coefficients $p(\Delta v, r_{\perp})_{\text{HI}} \geq 0.75$, with a median of 0.94. All but three of the molecular clouds have correlation coefficients greater than 0.5, and a median of $p(\Delta v, r_{\perp})_{\text{HI}} \approx 0.74$. This demonstrates that the velocity fields of both populations are reasonably well-approximated by a planar model, justifying the use of the large-scale gradients derived from plane-fitting to describe their kinematics. (Note that the large-scale gradient in the cloud velocity fields need not be due to rotation; Ω can be used to reproduce the distribution of j in a population (Burkert & Bodenheimer 2000).)

5. ANGULAR MOMENTUM

The angular momentum of a rotating body is given by:

$$J = I\omega = cMR^2\Omega, \quad (9)$$

where the angular velocity, ω , can be replaced by the velocity gradient, Ω , for solid-body rotation ($dv/dR =$

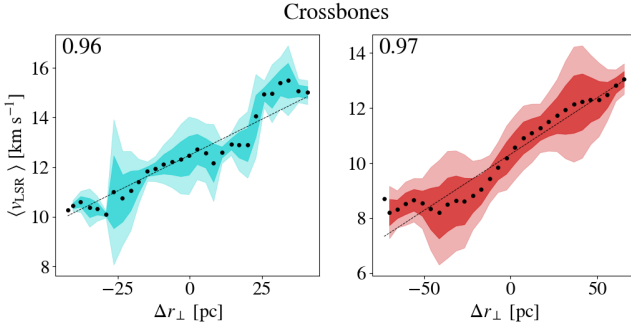


Figure 5. First moment velocity centroid, $\langle v \rangle$, as a function of the perpendicular displacement, r_\perp , from the rotation axis of the Crossbones molecular cloud (*left*) and its HI envelope (*right*). The dashed lines indicate the planar model, and the shaded regions show the $\pm 1\sigma$ and $\pm 2\sigma$ standard deviation of the velocity field map at each radial bin. The Pearson correlation coefficient of each cloud is in the upper left corner of each plot.

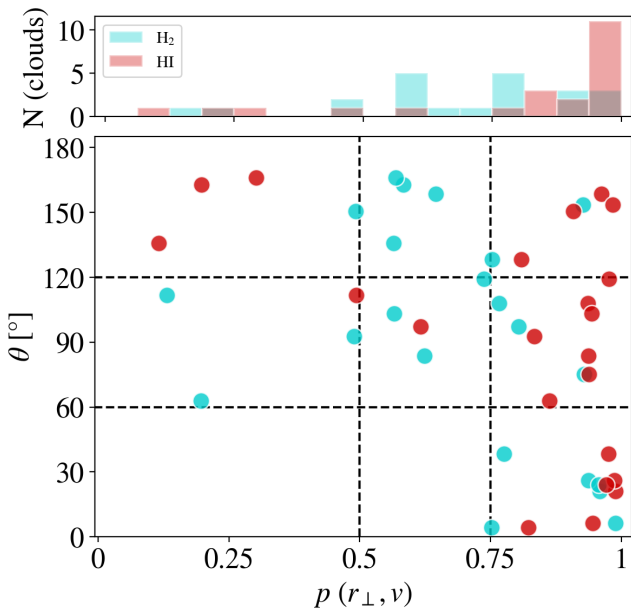


Figure 6. Pearson correlation coefficients of the molecular clouds (cyan) and the HI envelopes (red) as a function of cloud latitude.

0). and c is an order-unity coefficient set by the body's shape, rotation axis, and density distribution. We adopt a value of $c = 0.4$, applicable to a uniform density sphere.

For an object whose primary rotation axis is in the plane of the sky, Ω would appear as a linear gradient in the velocity field. Then the rotational angular momentum per unit mass is given by:

$$j \equiv \frac{J}{M} = cR^2\Omega. \quad (10)$$

In the following section, we present our measurements of the specific angular momenta of the two phases, j_{H_2} and j_{HI} . We then discuss how they compare with each other, as well as with the observations in the literature.

5.1. Specific Angular Momentum

The molecular clouds have specific angular momenta in the range $j_{H_2} \in (2.2 \times 10^{23} - 5.1 \times 10^{25}) \text{ cm}^2 \text{ s}^{-1}$, with a median value of $3.9 \times 10^{24} \text{ cm}^2 \text{ s}^{-1}$. On the other hand, the HI envelopes have $j_{HI} \in (1.4 \times 10^{24} - 1.6 \times 10^{26}) \text{ cm}^2 \text{ s}^{-1}$, with a median of $1.6 \times 10^{25} \text{ cm}^2 \text{ s}^{-1}$. Moreover, we find that the ratio of the specific angular momenta of the two phases, j_{HI}/j_{H_2} , spans $0.6 - 32$, with an average of 5. This is about twice as large as what IB measure for clouds in the Milky Way ($j_{HI}/j_{H_2} \approx 3$) and about a fifth of what IBB find for M33 clouds ($j_{HI}/j_{H_2} \approx 27$). We fit our data and find that the ratio of angular momenta scales as $j_{HI}/j_{H_2} \propto j_{H_2}^{-0.32 \pm 0.14}$ (Figure 4). On the other hand, IBB determine a steeper relation, $j_{HI} \propto j_{H_2}^{-1.17 \pm 0.05}$.

The angular momentum problem which IB demonstrated in the Milky Way persists in this work, and has in fact been exacerbated. IB used masses calculated from the optically thick ^{12}CO line. For the velocity fields, they used ^{13}CO , since the narrower linewidth enables finer velocity resolution. For each of the five clouds in common—Perseus, Orion A, Mon OB1, Mon R2, and Rosette—we measure masses that are from ~ 2.4 to 4.1 times higher than IB. This leads to the HI accumulation radii we calculate being on average $1.3 \times$ larger; which in turn results in larger HI masses. Our redefinition of the atomic gas accumulation radius (assuming spherical instead of cylindrical geometry) also plays a role in increasing the HI masses, since at a fixed volume, the radius of a sphere would be 1.5 times larger than that of a cylinder.

While IB had asserted that large-scale velocity gradients measured using ^{13}CO and ^{12}CO are consistent with one another, our measurements of Ω_{H_2} are systematically larger than what they obtain from ^{13}CO observations. Nevertheless, the average j_{HI}/j_{H_2} that we measure for the 5 clouds is larger than what IB found, due to the larger HI accumulation radii, discussed above.

5.2. Scaling Relations

Turbulence plays a key role in supporting molecular clouds against gravitational collapse (e.g., Larson 1981). This turbulence is primarily supersonic, following a size-linewidth scaling of $\sigma \propto R^{1/2}$ (Burkert & Bodenheimer 2000). The angular velocity of a cloud and its linewidth scale as $\Omega \propto \sigma/R$, implying a specific angular momentum-size relation of $j \propto R^{3/2}$ (Burkert & Bodenheimer 2000).

Least-squares fitting to our measurements shows that the molecular clouds have specific angular momenta that scale as $j_{\text{H}_2} \propto R^{1.68 \pm 0.21}$. The HI envelope follow a similar scaling $j_{\text{HI}} \propto R^{1.67 \pm 0.24}$, both of which are within 2σ of the $j \propto R^{1.5}$ relation expected of a supersonic turbulent cascade (Figure 10).

To examine the evolution of specific angular momentum across size scales—from the substructure in molecular clouds to the atomic envelopes encompassing them—we place our results next to previous observations of star-forming regions. Phillips (1999) compiled three-decades worth of observations of molecular cloud structures, while more recent observations of cores, the immediate precursors to stars, were conducted by Chen et al. 2007; Tatematsu et al. 2016; Chen et al. 2019). With the results from this study, we show that molecular clouds and cores across four orders of magnitude in size ($10^{-2} - 10^2$ pc) follow a power-law relationship of $j \propto R^{1.42 \pm 0.03}$ (Figure 10). This suggests that a turbulence cascade exists in the Galaxy spanning from dense pre-stellar cores to diffuse atomic clouds.

6. DISCUSSION

We now describe a simple physical model describing angular momentum transport that occurs during the formation of a molecular cloud. We calculate the properties of the progenitor atomic gas from which a molecular

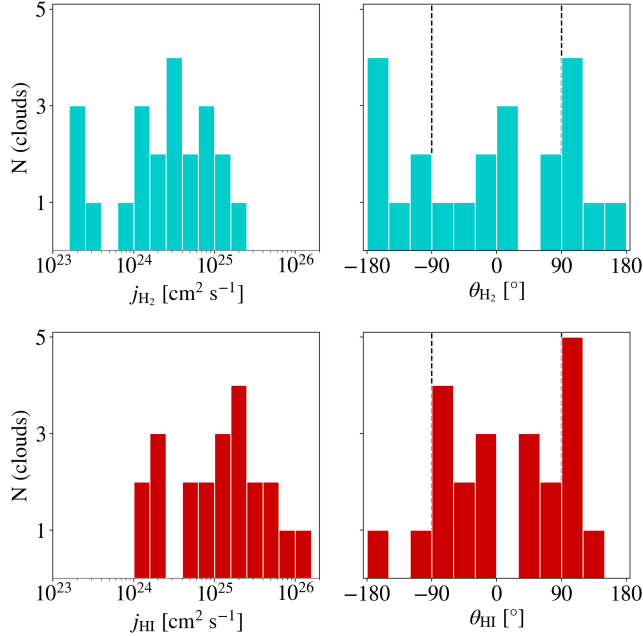


Figure 7. Angular momenta of the molecular clouds (first row) and HI envelopes (second row). The left column shows the specific angular momentum of each population and the right column shows the position angle of the angular momenta.

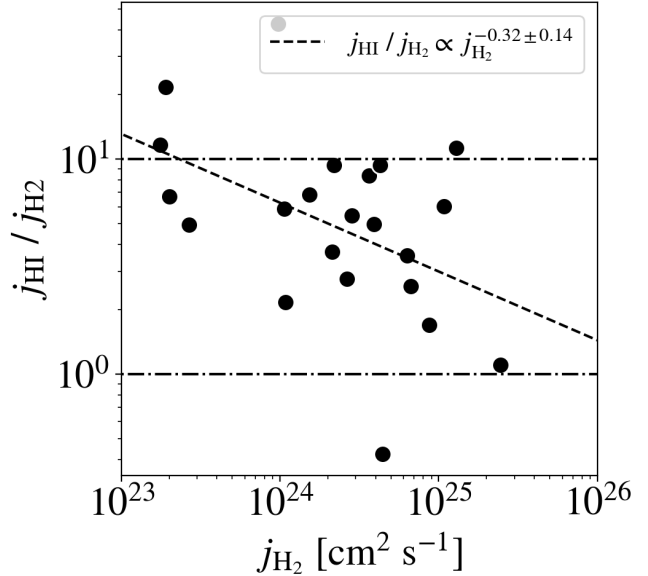


Figure 8. Ratio of the specific angular momentum of HI envelopes with respect to those of their corresponding molecular clouds.

cloud forms. We also calculate the timescale for angular momentum redistribution and analyze the motion of HI envelopes within the context of the Galaxy.

6.1. Estimating Momentum Transport Timescales

Magnetohydrodynamical simulations of molecular cloud formation show that as gas collapses, angular momentum from dense, molecular clouds is transported into the surrounding diffuse atomic gas (e.g., Arroyo-Chávez & Vázquez-Semadeni 2022, Misugi et al. 2024). Below, we describe the molecular cloud and HI envelope as a co-evolving system with a shared common progenitor, in order to estimate the timescale for angular momentum transport in molecular clouds.

Assuming conservation of angular momentum of the initial (pre-molecular cloud) system, we write:

$$J_{\text{total}} = J_{\text{HI}} + J_{\text{H}_2} = J_{\text{init}} \quad (11)$$

where, J_{HI} and J_{H_2} are the total angular momenta of the present HI envelope and molecular cloud respectively and J_{init} is the total angular momentum of the progenitor, assuming the conservation of angular momentum in the system. The specific angular momentum of the original system is:

$$j_{\text{init}} = \frac{M_{\text{H}_2} j_{\text{H}_2} + M_{\text{HI}} j_{\text{HI}}}{M_{\text{H}_2} + M_{\text{HI}}} \quad (12)$$

The progenitor HI clouds of the systems we study here have angular momenta of $j_{\text{init}} \in (1.2 \times 10^{24}, 1.3 \times 10^{26}) \text{ cm}^2 \text{ s}^{-1}$, with a median of $1.3 \times 10^{25} \text{ cm}^2 \text{ s}^{-1}$.

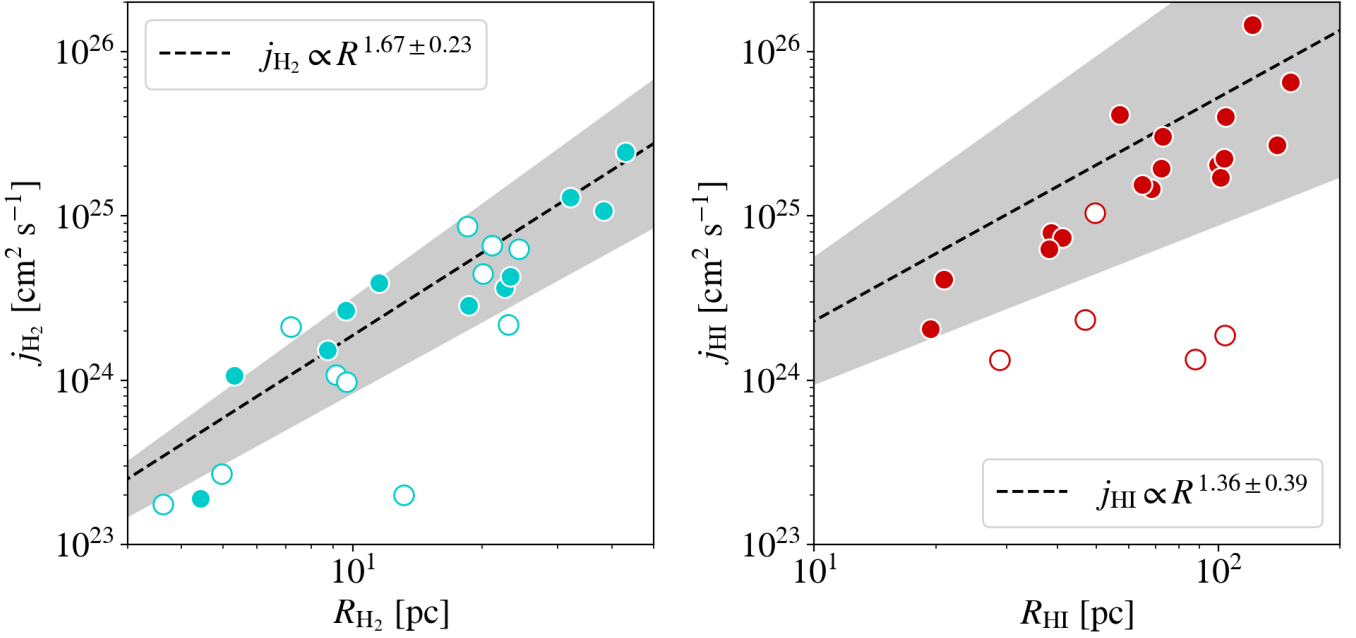


Figure 9. The specific angular momentum of molecular clouds (*left*) and their HI envelopes (*right*) as a function of size. The dashed lines are the least-squares fit to the data, and the shaded regions indicate the $\pm 1\sigma$ error of each fit. In each panel, the un-filled data points correspond to a Pearson coefficient of < 0.75 (Section 4.1)

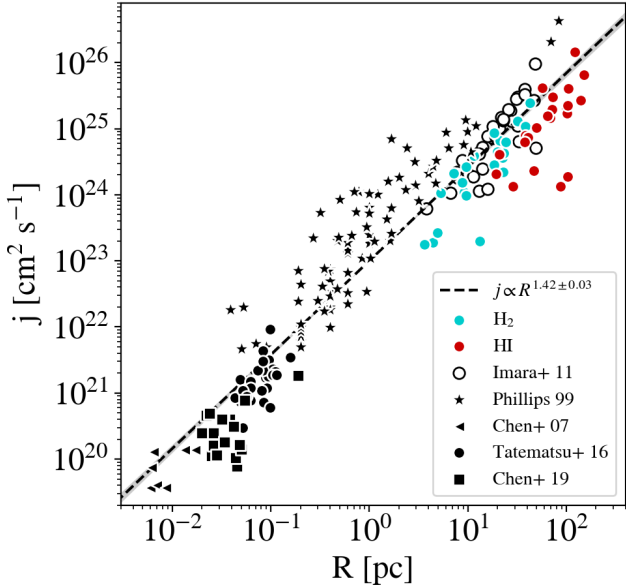


Figure 10. Size-Angular Momentum relation of star-forming regions in the Solar Neighborhood; a supersonic turbulent cascade is observed in the size range $10^{-2} < R < 10^2$ pc

The progenitor clouds have specific angular momenta that are ≈ 5 times larger than j_{H_2} , which puts them as intermediate between the present day molecular cloud and HI envelope (Figure 11). This may suggest that

the increase from j_{init} to j_{HI} is caused by the molecular cloud redistributing angular momentum as it forms.

To estimate the timescale over which the angular momentum of the progenitor system is transported away from the molecular cloud, we assume that the dominant torque for redistributing angular momentum also dissipates energy from the system. By dimensional analysis, the angular momentum dissipation rate can be written as $\Delta J / \Delta t_{diss} \approx \Delta E$. We then express the redistribution timescale Δt_{diss} in terms of observationally-derived quantities:

$$\Delta t_{diss} = \frac{J_{HI}}{E_{HI}} = \frac{j_{HI}}{e_{HI}} \quad (13)$$

Above, we have assumed that total change in angular momentum ΔJ reduces to $\Delta J = J_{init} - J_{H_2} = J_{HI}$, and that the same logic applies to the total change in energy: $\Delta E = E_{HI}$. The total specific energy e_{HI} is calculated as the sum of gravitational, rotational and turbulent energies of the HI envelope:

$$e_{HI} \approx -\frac{GM}{R} + (\Omega R)^2 + \sigma^2 \quad (14)$$

All but two of the molecular clouds have redistribution timescales $\Delta t_{dis} < 2$ Myr, with a median of 0.68 Myr (Figure 11). This is ≈ 9 (21) times smaller than the average free-fall time of the molecular clouds (HI envelopes), which may suggest that angular momentum redistribution has opportunity to brake the gas and facilitate gravitational collapse, in tandem with the increased pressure

from the transition to colder and denser phases (e.g., Blitz & Rosolowsky 2006).

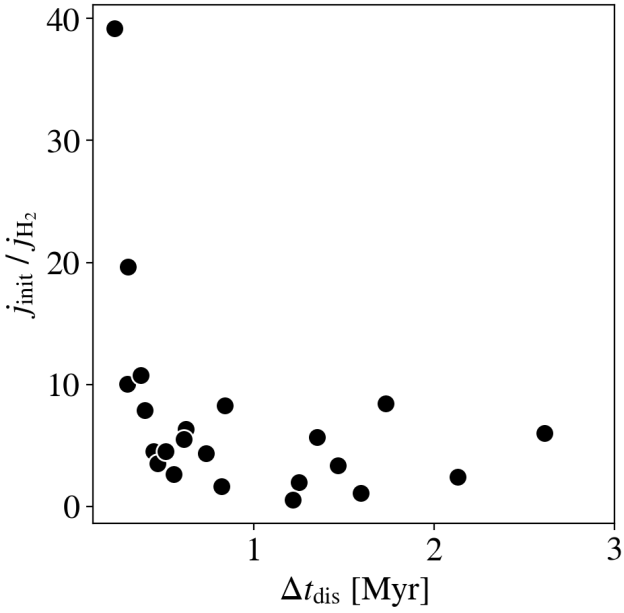


Figure 11. Ratio of the initial and present-day angular momenta of the molecular clouds, as a function of the redistribution timescale.

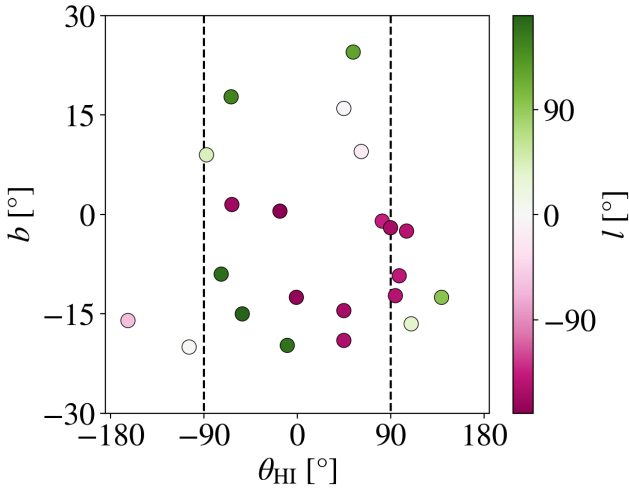


Figure 12. Velocity gradient position angles of the HI envelopes, arranged according to Galactic latitude. The colorbar indicates the Galactic longitude coordinates of each envelope.

6.2. Cloud Motion in the Context of the Galaxy

The position angles of the molecular cloud velocity gradients are evenly distributed (Figure 7). About 9 (40%) of the molecular clouds are rotating in the same

sense as the Galaxy ($|\theta| < 90^\circ$), with the remaining 13 are having position angles that differ from the Galaxy by more than 90° . On the other hand, almost two-thirds of the HI envelopes are co-rotating with respect to the Galaxy. More than half (12) of the HI clouds have vertical velocity gradients ($\theta \in 90^\circ \pm 30^\circ$).

If Ω_{HI} arose due to rotation, our measurements would imply that more than half of HI envelopes would have rotation planes that are perpendicular to large-scale rotation. This seems surprising given the dynamical coupling of HI clouds to the Galaxy (e.g., Jeffreson et al. 2020). Further examination shows that 5 of these HI envelopes share similar on-sky coordinates (Figure 12), with the overlap among their velocity fields artificially increasing the occurrence rate of vertical velocity gradients.

Future work can improve upon this by distinguishing between molecular clouds that might share a common HI envelope, and those where the overlap is due to chance. The former will require refining our model of angular momentum redistribution to account to account for the co-evolution of multiple molecular regions with one another. For those clouds whose HI envelopes overlap purely due to projection, the velocity fields of the fore- and background systems need to be disentangled. This necessitates characterizing the distribution of emitting material along the line-of-sight, e.g., using dust-derived three-dimensional reconstructions of the Solar Neighborhood such as those by Dharmawardena et al. 2024; Edenhofer et al. 2024; Leike et al. 2020.

7. SUMMARY AND CONCLUSIONS

With the aim of investigating the angular momentum in molecular clouds and their associated HI envelopes, we identify atomic gas associated with 22 molecular clouds in the Solar Neighborhood following Imara & Blitz (2011) and Imara et al. (2011).

- We measure the properties of the molecular clouds and their associated HI envelopes using ^{12}CO and 21-cm observations. The accumulation radii of the HI envelopes are on average 4 times the size, and 8 times more massive compared to their corresponding molecular cloud.
- The velocity field maps of both populations are fit with planes to derive the large-scale velocity gradients, Ω_{HI} and Ω_{H_2} (Figure 3). The molecular clouds have typical velocity gradients of $\Omega_{\text{H}_2} \approx 0.12 \text{ km s}^{-1} \text{ pc}^{-1}$, while the HI have gradients of $\Omega_{\text{HI}} \approx 0.03 \text{ km s}^{-1}$. The rotation axes of the molecular clouds and their HI envelopes tend to be unaligned, with $\Delta\theta$ ranging uniformly between 0° and 180° .

- The average specific angular momentum of the HI envelopes is $j_{\text{HI}} \approx 2.5 \times 10^{25} \text{ cm}^2 \text{ s}^{-1}$, which is on average 5 times larger than the corresponding j_{H_2} (Figure 8). Along with the abundance of systems with the random distribution of angular separations, this result suggests that angular momentum redistribution has occurred following the formation of molecular clouds.
- The specific angular momentum of molecular clouds scales with size as $j_{\text{H}_2} \propto R^{1.67 \pm 0.23}$, while the HI envelopes follow a steeper relation of $j_{\text{HI}} \propto R^{1.36 \pm 0.39}$. Both are consistent with the $j \propto R^{1.5}$ scaling expected of a supersonic turbulence cascade. We also demonstrate that a supersonic turbulent cascade extends over four orders of magnitude in size (Figure 10).
- We develop a simple physical model describing the coevolution of the molecular and atomic phases,

and estimate the specific angular momentum of the progenitor HI cloud from which the present-day molecular cloud-HI envelope system formed. We use also this model to derive the timescales over which angular momentum is redistributed from the molecular clouds to their surrounding HI, and find $\Delta t_{\text{dis}} \sim 0.9 \text{ Myr}$ (Figure 11).

We are grateful to John Forbes, Erich Koch, Chris McKee, and Karin Sandstrom for insightful discussions that helped to improve this paper. We also thank an anonymous referee for their constructive feedback. We acknowledge support from the Heising-Simons Foundation (grant 2022-3532) for this work.

Software: astropy (Astropy Collaboration et al. 2013, 2018, 2022), matplotlib (Developers 2016), pandas (Reback et al. 2022) scipy (Virtanen et al. 2018) numpy (Harris et al. 2020)

REFERENCES

- Arroyo-Chávez, G., & Vázquez-Semadeni, E. 2022, ApJ, 925, 78, doi: [10.3847/1538-4357/ac3915](https://doi.org/10.3847/1538-4357/ac3915)
- Astropy Collaboration, Robitaille, T. P., Tollerud, E. J., et al. 2013, A&A, 558, A33, doi: [10.1051/0004-6361/201322068](https://doi.org/10.1051/0004-6361/201322068)
- Astropy Collaboration, Price-Whelan, A. M., Sipőcz, B. M., et al. 2018, AJ, 156, 123, doi: [10.3847/1538-3881/aabc4f](https://doi.org/10.3847/1538-3881/aabc4f)
- Astropy Collaboration, Price-Whelan, A. M., Lim, P. L., et al. 2022, ApJ, 935, 167, doi: [10.3847/1538-4357/ac7c74](https://doi.org/10.3847/1538-4357/ac7c74)
- Blitz, L., & Rosolowsky, E. 2006, ApJ, 650, 933, doi: [10.1086/505417](https://doi.org/10.1086/505417)
- Braine, J., Hughes, A., Rosolowsky, E., et al. 2020, A&A, 633, A17, doi: [10.1051/0004-6361/201834613](https://doi.org/10.1051/0004-6361/201834613)
- Braine, J., Rosolowsky, E., Gratier, P., Corbelli, E., & Schuster, K. F. 2018, A&A, 612, A51, doi: [10.1051/0004-6361/201732405](https://doi.org/10.1051/0004-6361/201732405)
- Burkert, A., & Bodenheimer, P. 2000, ApJ, 543, 822, doi: [10.1086/317122](https://doi.org/10.1086/317122)
- Chen, H. H.-H., Pineda, J. E., Offner, S. S. R., et al. 2019, ApJ, 886, 119, doi: [10.3847/1538-4357/ab4ce9](https://doi.org/10.3847/1538-4357/ab4ce9)
- Chen, X., Launhardt, R., & Henning, T. 2007, ApJ, 669, 1058, doi: [10.1086/521868](https://doi.org/10.1086/521868)
- Dame, T. M. 2011, arXiv e-prints, arXiv:1101.1499, doi: [10.48550/arXiv.1101.1499](https://doi.org/10.48550/arXiv.1101.1499)
- Dame, T. M., Hartmann, D., & Thaddeus, P. 2001, ApJ, 547, 792, doi: [10.1086/318388](https://doi.org/10.1086/318388)
- Developers, M. 2016, matplotlib: v1.5.3, v1.5.3, Zenodo, doi: [10.5281/zenodo.61948](https://doi.org/10.5281/zenodo.61948)
- Dharmawardena, T. E., Bailer-Jones, C. A. L., Fouesneau, M., et al. 2024, MNRAS, 532, 3480, doi: [10.1093/mnras/stae1474](https://doi.org/10.1093/mnras/stae1474)
- Edenhofer, G., Zucker, C., Frank, P., et al. 2024, A&A, 685, A82, doi: [10.1051/0004-6361/202347628](https://doi.org/10.1051/0004-6361/202347628)
- Goodman, A. A., Benson, P. J., Fuller, G. A., & Myers, P. C. 1993, ApJ, 406, 528, doi: [10.1086/172465](https://doi.org/10.1086/172465)
- Harris, C. R., Millman, K. J., van der Walt, S. J., et al. 2020, Nature, 585, 357, doi: [10.1038/s41586-020-2649-2](https://doi.org/10.1038/s41586-020-2649-2)
- HI4PI Collaboration, Ben Bekhti, N., Flöer, L., et al. 2016, A&A, 594, A116, doi: [10.1051/0004-6361/201629178](https://doi.org/10.1051/0004-6361/201629178)
- Imara, N., Bigiel, F., & Blitz, L. 2011, ApJ, 732, 79, doi: [10.1088/0004-637X/732/2/79](https://doi.org/10.1088/0004-637X/732/2/79)
- Imara, N., & Blitz, L. 2011, ApJ, 732, 78, doi: [10.1088/0004-637X/732/2/78](https://doi.org/10.1088/0004-637X/732/2/78)
- Imara, N., & Burkhardt, B. 2016, ApJ, 829, 102, doi: [10.3847/0004-637X/829/2/102](https://doi.org/10.3847/0004-637X/829/2/102)
- Jeffreson, S. M. R., Kruijssen, J. M. D., Keller, B. W., Chevance, M., & Glover, S. C. O. 2020, Monthly Notices of the Royal Astronomical Society, 498, 385–429, doi: [10.1093/mnras/staa2127](https://doi.org/10.1093/mnras/staa2127)
- Kalberla, P. M. W., Burton, W. B., Hartmann, D., et al. 2005, A&A, 440, 775, doi: [10.1051/0004-6361:20041864](https://doi.org/10.1051/0004-6361:20041864)
- Krumholz, M. R., McKee, C. F., & Tumlinson, J. 2009, ApJ, 693, 216, doi: [10.1088/0004-637X/693/1/216](https://doi.org/10.1088/0004-637X/693/1/216)
- Kutner, M. L., Tucker, K. D., Chin, G., & Thaddeus, P. 1977, ApJ, 215, 521, doi: [10.1086/155384](https://doi.org/10.1086/155384)

- 609 Larson, R. B. 1981, MNRAS, 194, 809,
 610 doi: [10.1093/mnras/194.4.809](https://doi.org/10.1093/mnras/194.4.809)
- 611 —. 1984, MNRAS, 206, 197, doi: [10.1093/mnras/206.1.197](https://doi.org/10.1093/mnras/206.1.197)
- 612 Leike, R. H., Glatzle, M., & Enßlin, T. A. 2020, A&A, 639,
 613 A138, doi: [10.1051/0004-6361/202038169](https://doi.org/10.1051/0004-6361/202038169)
- 614 Lewis, J. A., Lada, C. J., & Dame, T. M. 2022, ApJ, 931, 9,
 615 doi: [10.3847/1538-4357/ac5d58](https://doi.org/10.3847/1538-4357/ac5d58)
- 616 Machida, M. N., Tomisaka, K., Matsumoto, T., & Inutsuka,
 617 S.-i. 2008, ApJ, 677, 327, doi: [10.1086/529133](https://doi.org/10.1086/529133)
- 618 Misugi, Y., Inutsuka, S.-i., Arzoumanian, D., & Tsukamoto,
 619 Y. 2024, ApJ, 963, 106, doi: [10.3847/1538-4357/ad1990](https://doi.org/10.3847/1538-4357/ad1990)
- 620 Mouschovias, T. C., & Paleologou, E. V. 1979, ApJ, 230,
 621 204, doi: [10.1086/157077](https://doi.org/10.1086/157077)
- 622 Park, G., Koo, B.-C., Kim, K.-T., & Elmegreen, B. 2023,
 623 ApJ, 955, 59, doi: [10.3847/1538-4357/acebda](https://doi.org/10.3847/1538-4357/acebda)
- 624 Phillips, J. P. 1999, A&AS, 134, 241,
 625 doi: [10.1051/aas:1999137](https://doi.org/10.1051/aas:1999137)
- 626 Reback, J., Jbrockmendel, McKinney, W., et al. 2022,
 627 pandas-dev/pandas: Pandas 1.4.1, v1.4.1, Zenodo,
 628 doi: [10.5281/zenodo.6053272](https://doi.org/10.5281/zenodo.6053272)
- 629 Rosolowsky, E., Engargiola, G., Plambeck, R., & Blitz, L.
 630 2003, ApJ, 599, 258, doi: [10.1086/379166](https://doi.org/10.1086/379166)
- 631 Saha, P., Roy, N., & Bhattacharya, M. 2018, MNRAS, 480,
 632 L126, doi: [10.1093/mnrasl/sly139](https://doi.org/10.1093/mnrasl/sly139)
- 633 Shen, Y.-F., Xu, Y., Wang, Y.-B., et al. 2025, ApJ, 988,
 634 125, doi: [10.3847/1538-4357/ade399](https://doi.org/10.3847/1538-4357/ade399)
- 635 Sternberg, A., Gurman, A., & Bialy, S. 2021, ApJ, 920, 83,
 636 doi: [10.3847/1538-4357/ac167b](https://doi.org/10.3847/1538-4357/ac167b)
- 637 Tatematsu, K., Ohashi, S., Sanhueza, P., et al. 2016, PASJ,
 638 68, 24, doi: [10.1093/pasj/psw002](https://doi.org/10.1093/pasj/psw002)
- 639 Vázquez-Semadeni, E., Palau, A., Gómez, G. C., et al.
 640 2024, arXiv e-prints, arXiv:2408.10406,
 641 doi: [10.48550/arXiv.2408.10406](https://doi.org/10.48550/arXiv.2408.10406)
- 642 Virtanen, P., Gommers, R., Burovski, E., et al. 2018,
 643 scipy/scipy: Scipy 1.1.0rc1, v1.1.0rc1, Zenodo,
 644 doi: [10.5281/zenodo.1218715](https://doi.org/10.5281/zenodo.1218715)
- 645 Wolfire, M. G., McKee, C. F., Hollenbach, D., & Tielens,
 646 A. G. G. M. 2003, ApJ, 587, 278, doi: [10.1086/368016](https://doi.org/10.1086/368016)
- 647 Yen, H.-W., & Lee, Y.-N. 2024, ApJL, 972, L27,
 648 doi: [10.3847/2041-8213/ad7263](https://doi.org/10.3847/2041-8213/ad7263)
- 649 Zucker, C., Speagle, J. S., Schlafly, E. F., et al. 2019, ApJ,
 650 879, 125, doi: [10.3847/1538-4357/ab2388](https://doi.org/10.3847/1538-4357/ab2388)

APPENDIX

651

A. VELOCITY SPECTRA

652

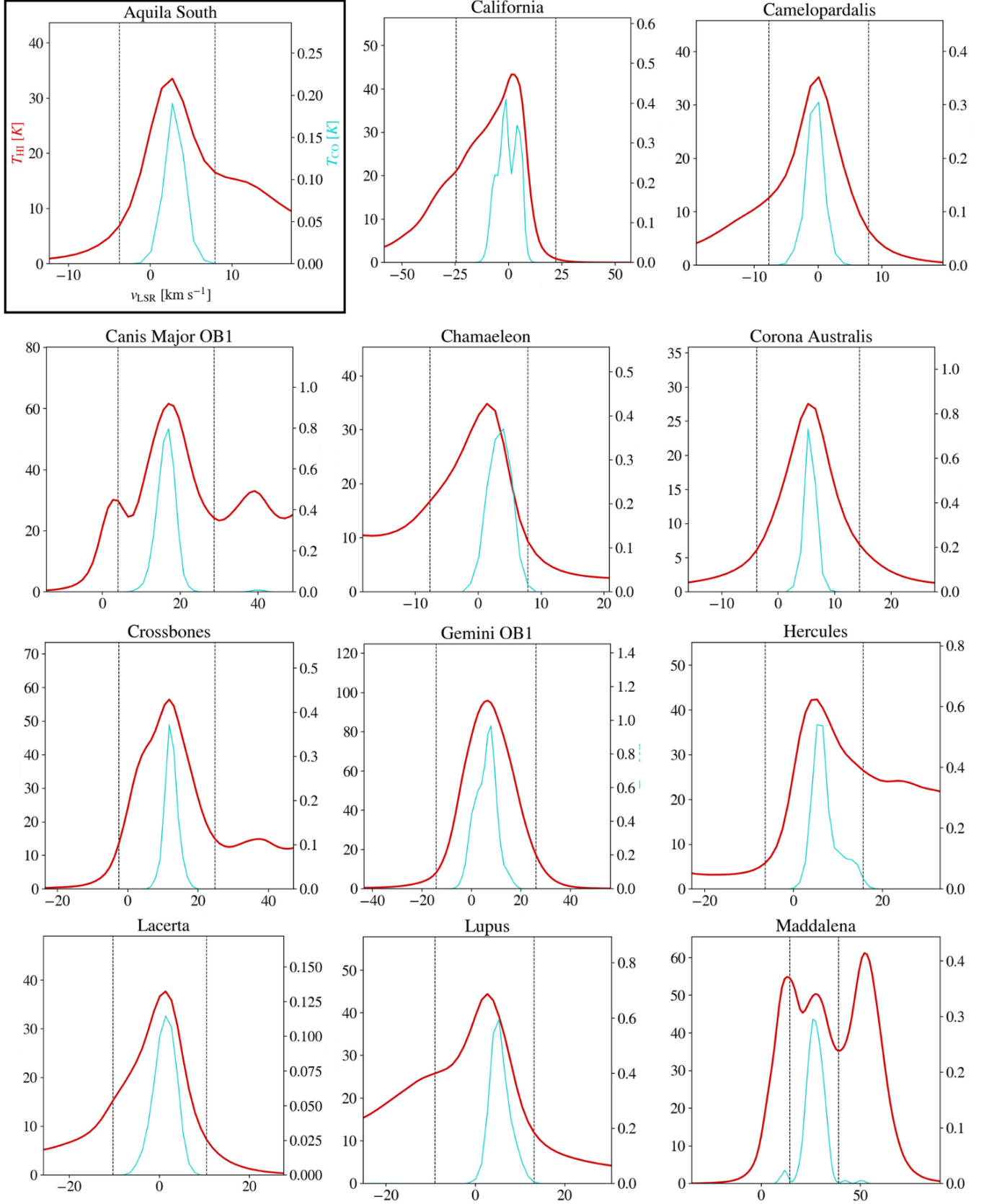


Figure 13. Velocity Spectra of the molecular clouds (cyan) and their associated HI envelopes (red) derived from ^{12}CO and 21-cm emission respectively.

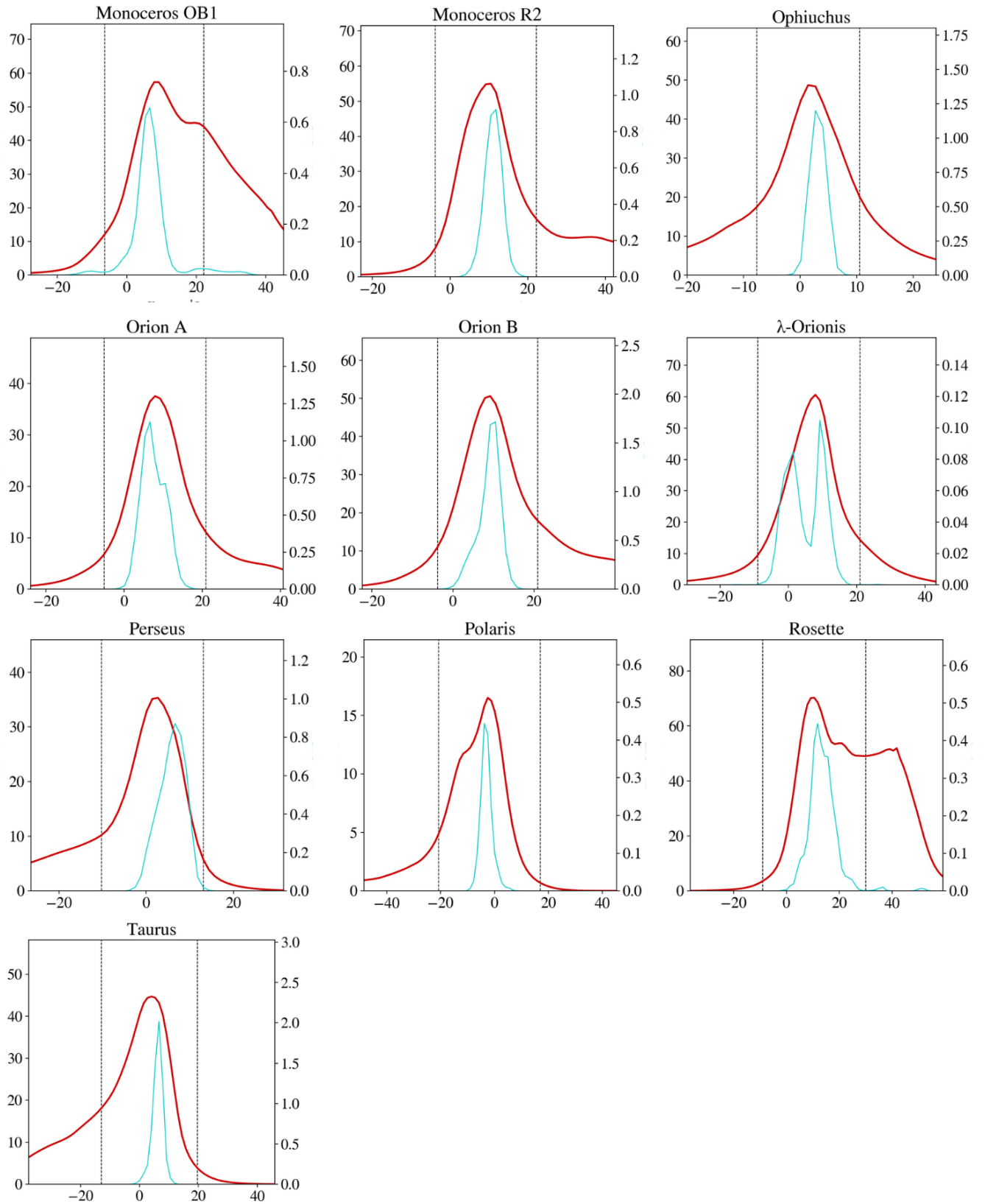


Figure 14. Same as Figure 13

B. SURFACE DENSITY AND VELOCITY MAPS

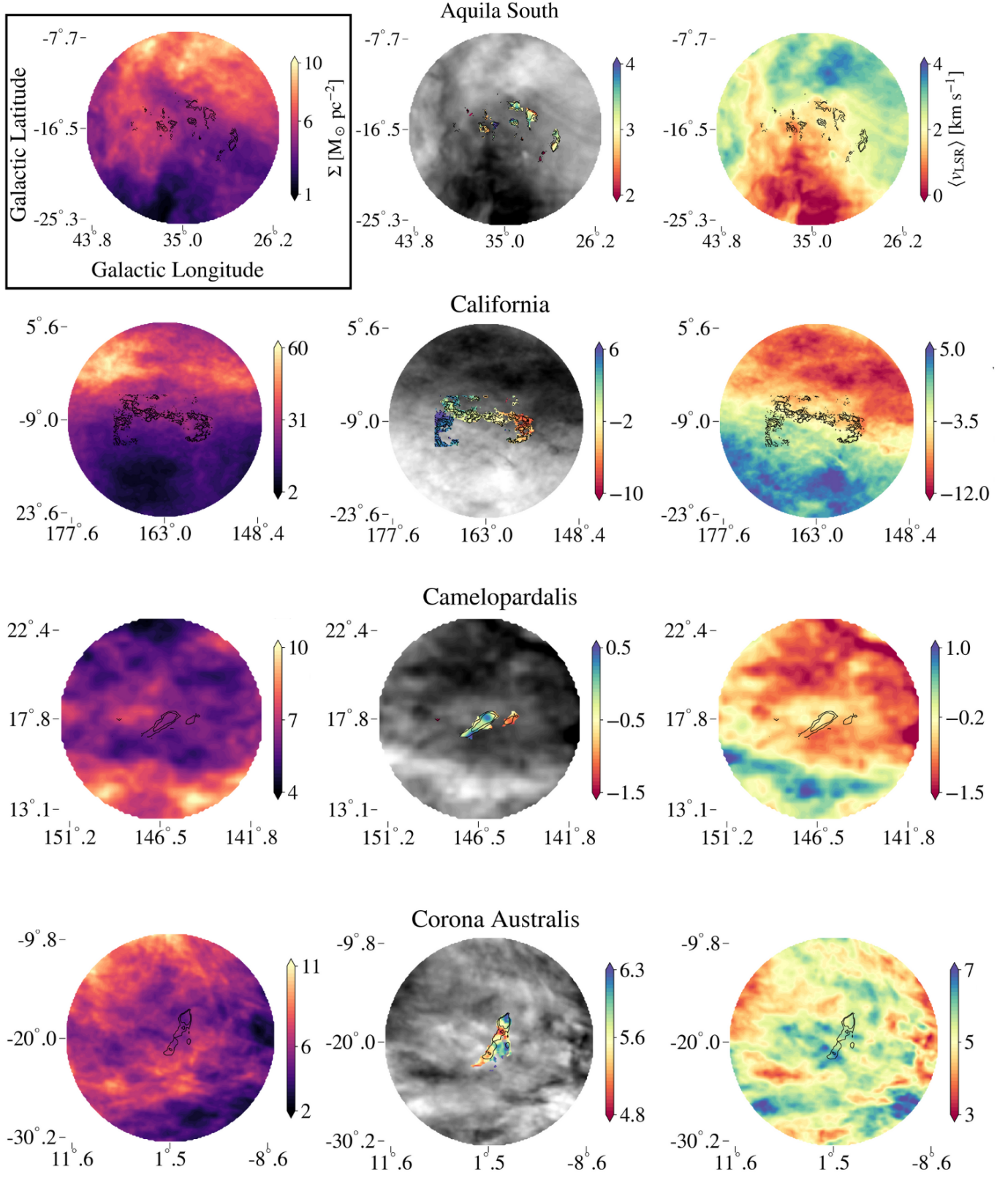


Figure 15. (Left) Surface density of the HI envelope, measured from integrating HI4PI over the spectral range defined by the Gaussian fit to the 21-cm spectra: $(\bar{v} \pm 2\sigma)_{\text{HI}}$ (Table 1). Velocity field maps of the molecular cloud (center) and HI envelope (right).

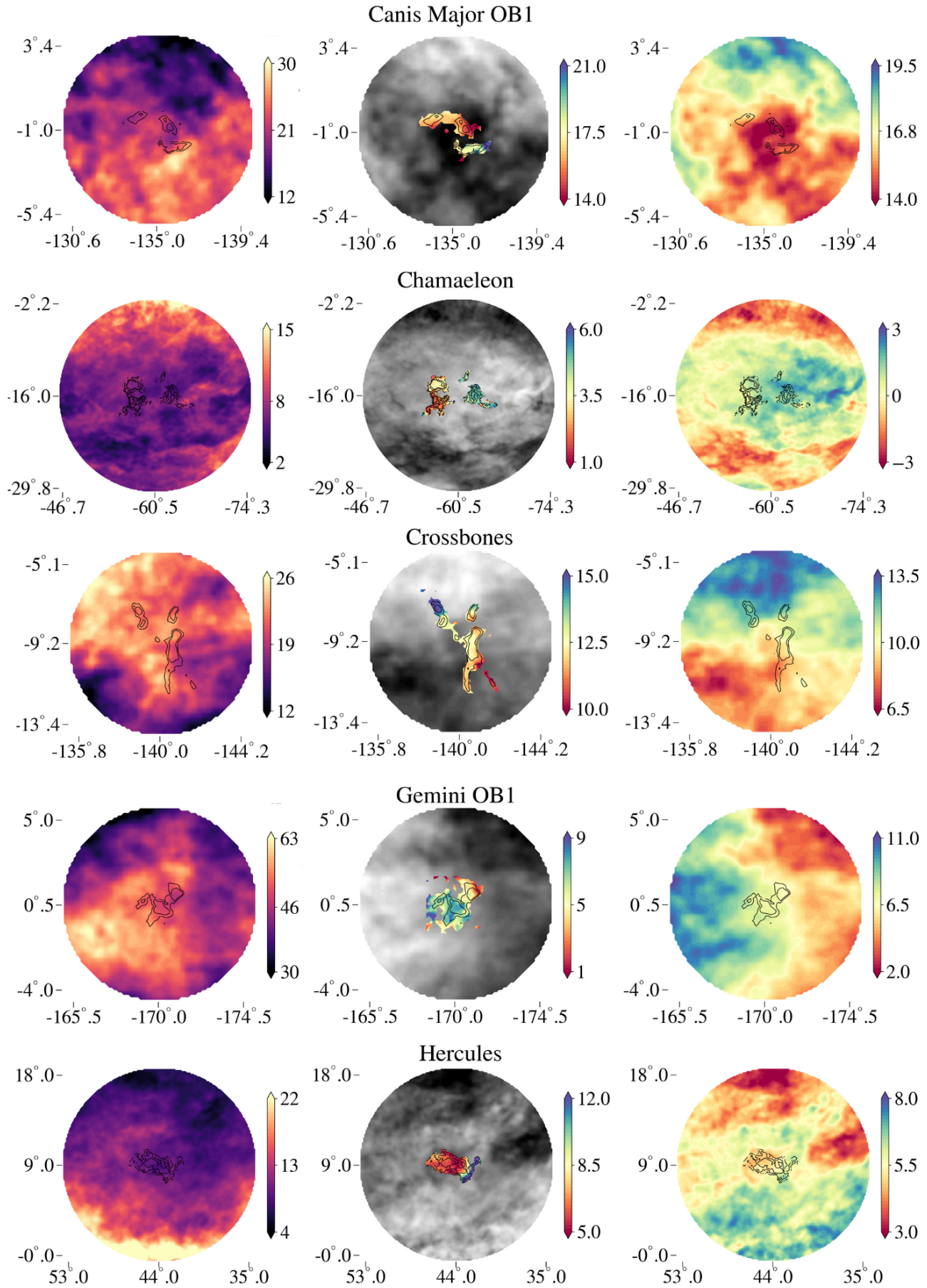


Figure 16. Same as Figure 15

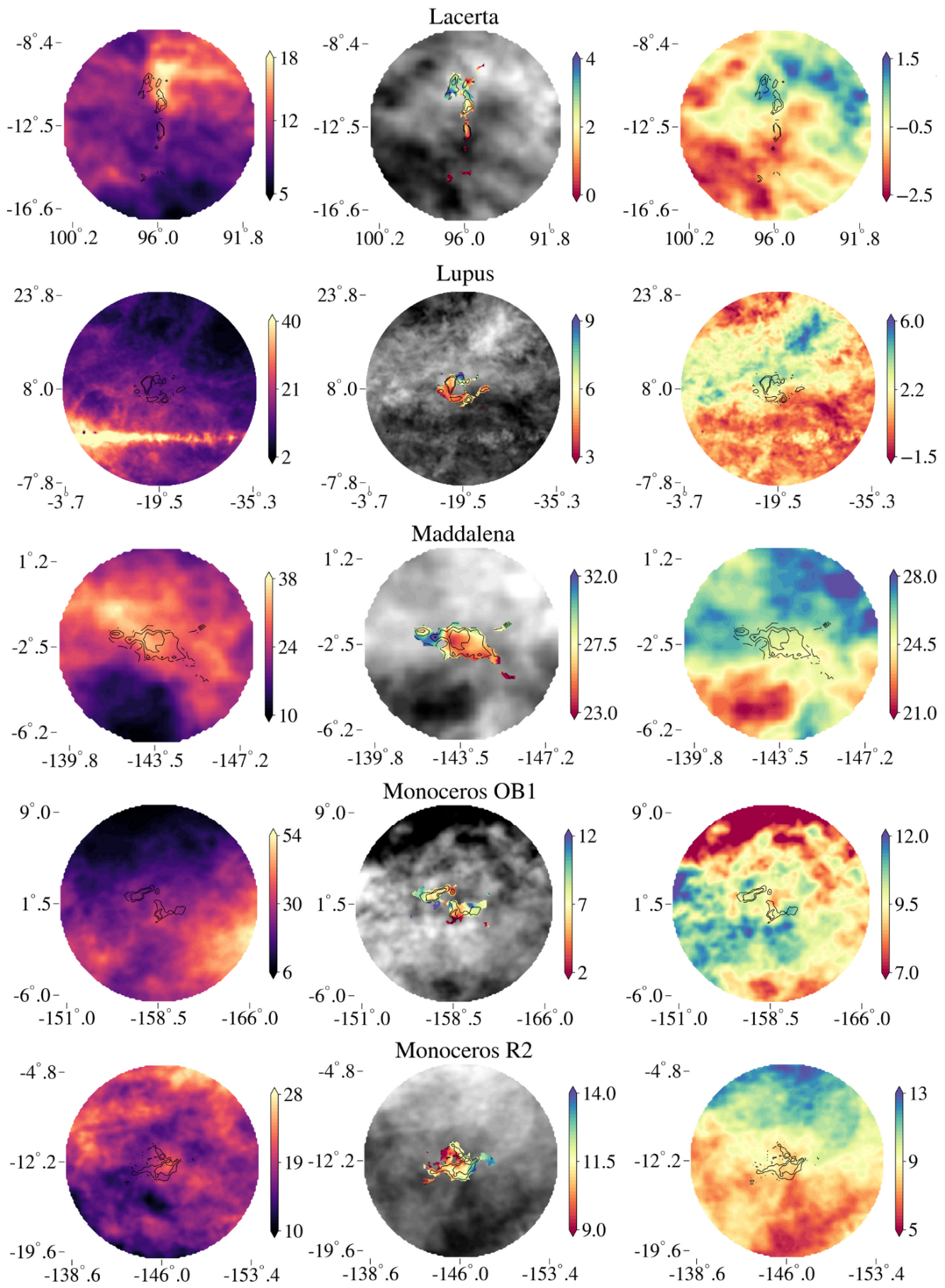


Figure 17. Same as Figure 15

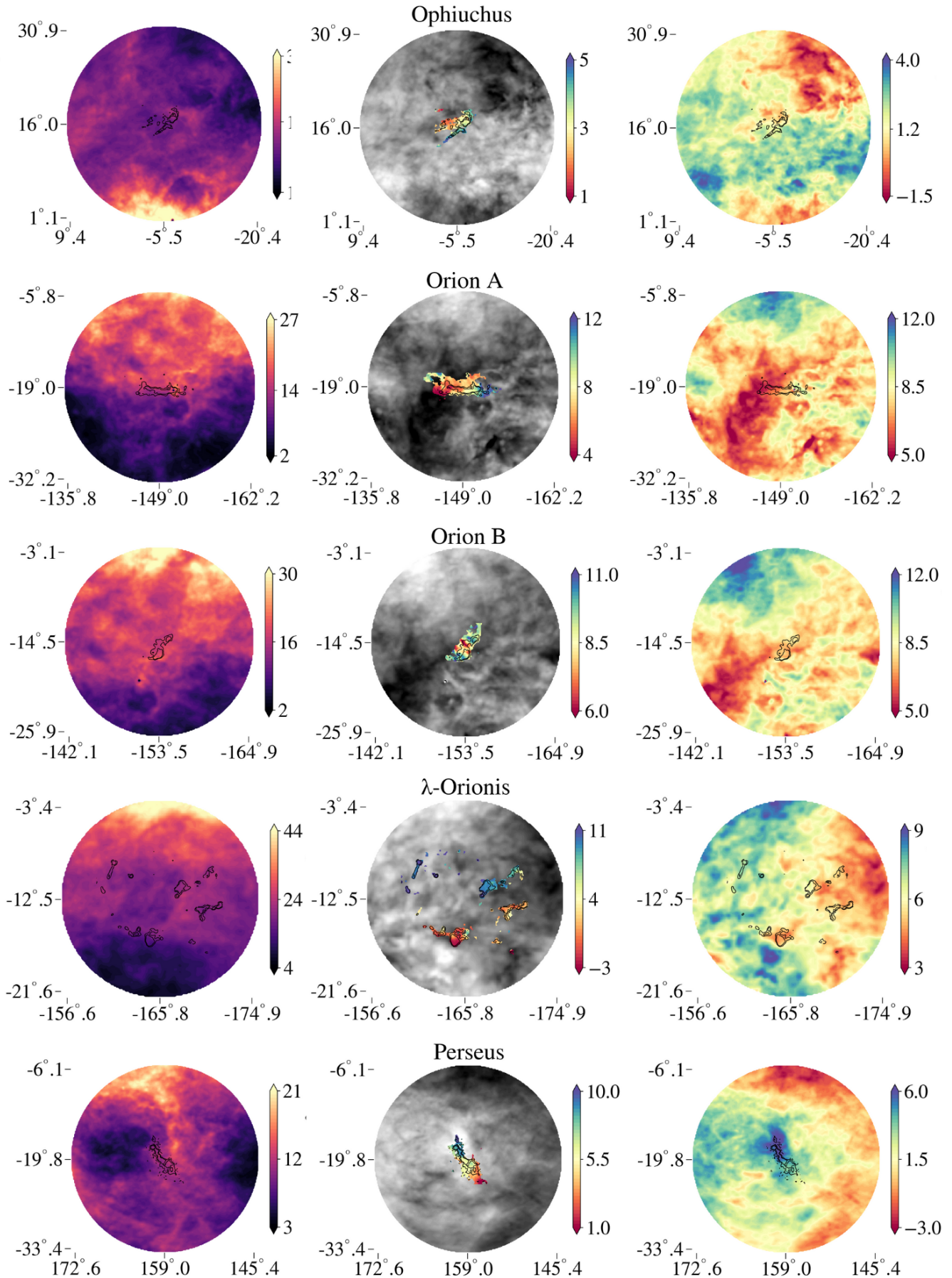


Figure 18. Same as Figure 15

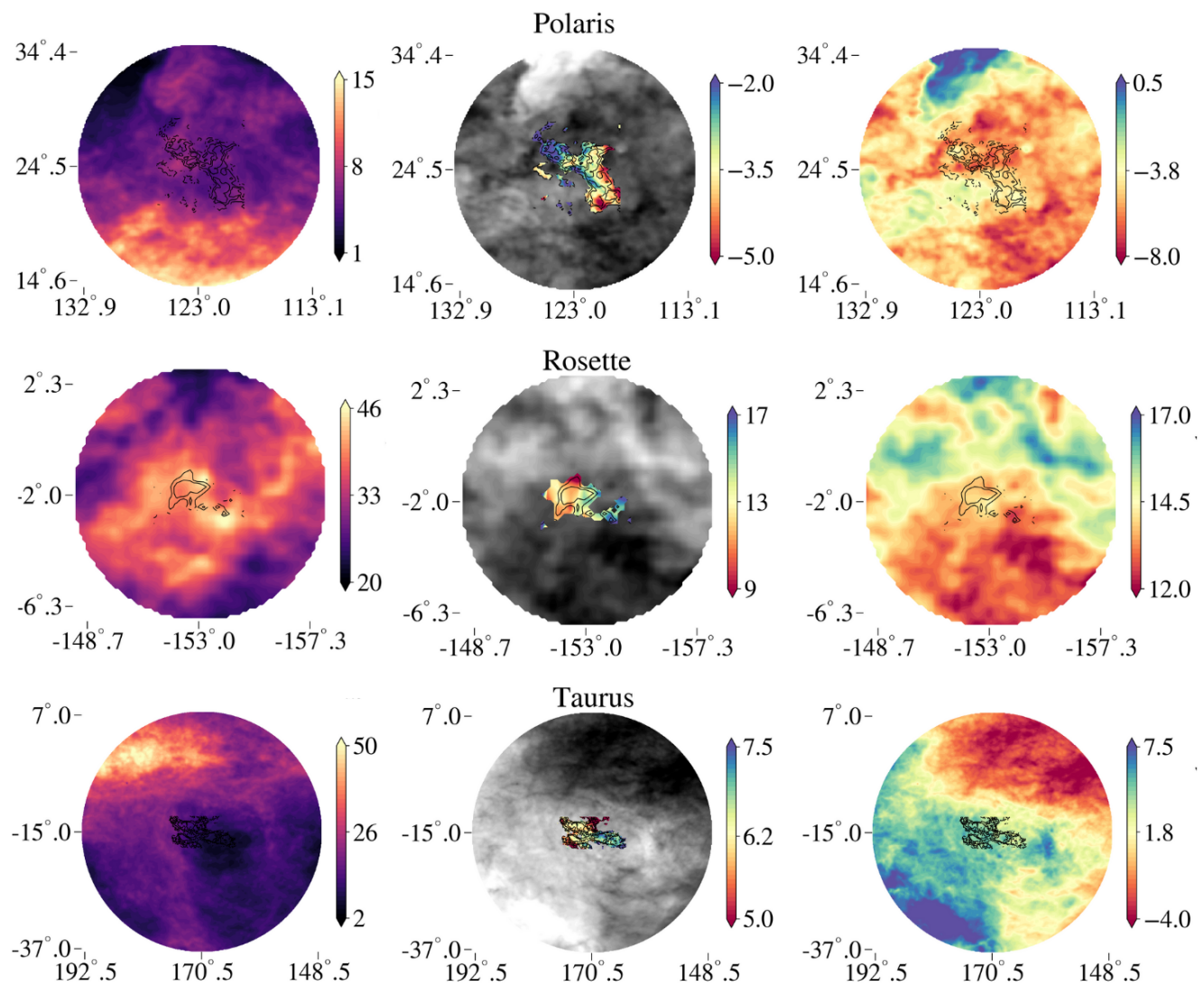


Figure 19. Same as Figure 15

C. VELOCITY PROFILES AS A FUNCTION OF PERPENDICULAR DISPLACEMENT

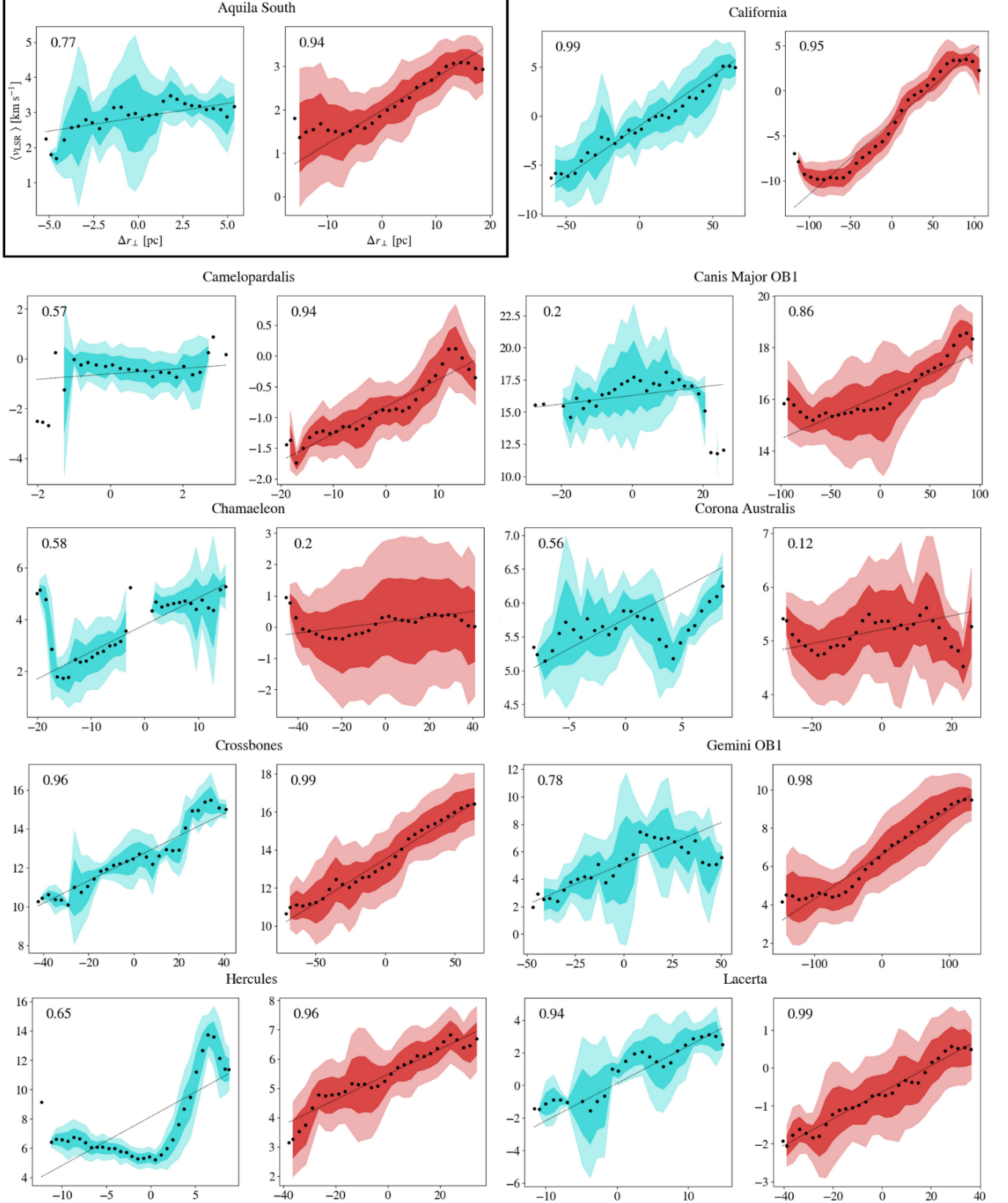


Figure 20. Intensity-weighted centroid velocity as a function of perpendicular distance from the rotation axis of the molecular clouds (

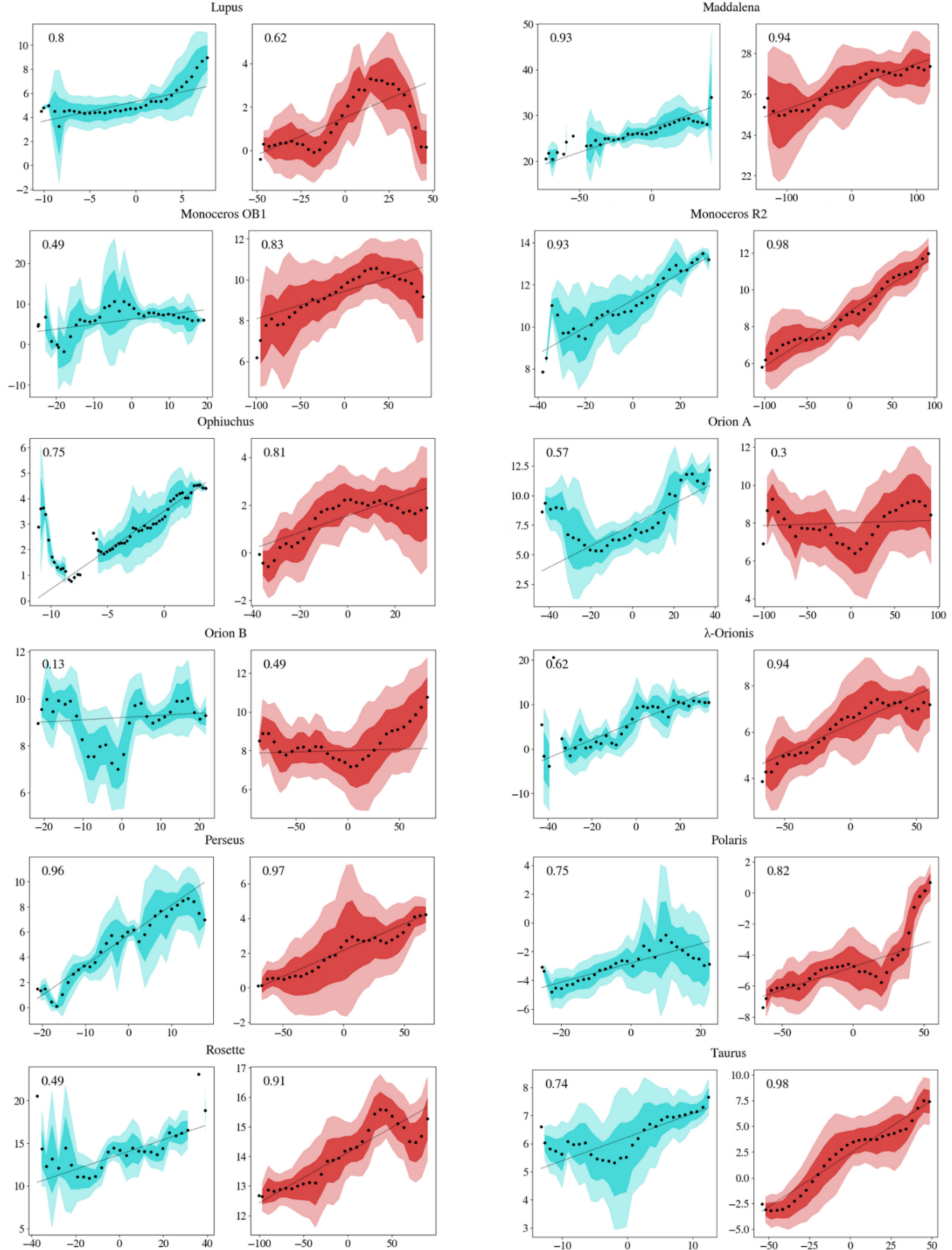


Figure 21. Same as Figure 20